

JGR Atmospheres

RESEARCH ARTICLE

10.1029/2020JD033055

Key Points:

- We present unique balloon-borne observations of stratospheric water vapor and aerosol backscatter above northern Scandinavia
- The balloon-borne measurements reveal Antarctic-like dehydration and rehydration and the existence of solid ice particles
- The far-ranging impact of Greenland's mountain wave-induced temperature fluctuations is a key process

Correspondence to:

R. Kivi,
rigel.kivi@fmi.fi

Citation:

Kivi, R., Dörnbrack, A., Sprenger, M., & Vömel, H. (2020). Far-ranging impact of mountain waves excited over Greenland on stratospheric dehydration and rehydration. *Journal of Geophysical Research: Atmospheres*, 125, e2020JD033055. <https://doi.org/10.1029/2020JD033055>

Received 11 MAY 2020

Accepted 14 AUG 2020

Accepted article online 29 AUG 2020

Far-Ranging Impact of Mountain Waves Excited Over Greenland on Stratospheric Dehydration and Rehydration

Rigel Kivi¹ , Andreas Dörnbrack² , Michael Sprenger³, and Holger Vömel⁴ 

¹Space and Earth Observation Centre, Finnish Meteorological Institute, Sodankylä, Finland, ²DLR Oberpfaffenhofen, Institut für Physik der Atmosphäre, Wessling, Germany, ³Institute for Atmospheric and Climate Science, ETH Zürich, Zürich, Switzerland, ⁴Earth Observing Laboratory, NCAR, Boulder, CO, USA

Abstract In situ observations of reduced stratospheric water vapor combined with those of ice particle formation are rarely conducted. On the one hand, they are essential to broaden our knowledge about the formation of polar stratospheric clouds (PSCs). On the other hand, the observed profiles allow the comparison with global circulation models. Here we report about a balloon-borne observation above Sodankylä, Finland on 26 January 2005. The frostpoint hygrometer detected layers of reduced water vapor by up to 2 ppmv from 18.5 to 23 km. Beneath, a 1-km-deep layer of increased water vapor was identified. An aerosol backscatter sonde measured the presence of stratospheric ice clouds. According to meteorological analysis the PSCs were formed upstream above the east coast of Greenland due to mountain wave-induced cooling. The inertia-gravity waves generated a large and persistent stratospheric wake far downstream of Greenland and led to the observed dehydration. Comparing the most recent ERA5 data with operational analyses from 2005, we find an improved representation of mesoscale internal gravity waves, dehydration and PSC formation for this particular event.

Plain Language Summary This paper investigates unique in situ observations of stratospheric water vapor and combines them with nearly simultaneous optical property measurements of ice particles. The presented results reveal Antarctic-like stratospheric dehydration and rehydration inside the Arctic polar vortex. Balloon-borne observations of this kind are extremely rare and constitute a valuable data set for extending our knowledge about both the cloud formation processes and the representation of water vapor in global circulation models. Here, we make use of state-of-the-art numerical weather prediction models with high spatial resolution. They allow to resolve dynamically processes that were not accessible when the observations were conducted in 2005. Besides the large-scale cooling inside the Arctic polar vortex, it is the far-ranging impact of the numerically resolved stratospheric mountain waves that was responsible for maintaining the thermodynamic conditions leading to the unique observations over Sodankylä, Finland.

1. Introduction

The water vapor concentration in the lower stratosphere can significantly influence the radiative forcing on the Earth's surface as well as stratospheric temperatures by modifying the infrared radiation (Forster & Shine, 1999, 2002; Khaykin et al., 2013; Solomon et al., 2010). These variations might cause circulation changes both in the stratosphere and troposphere (Maycock et al., 2013, 2014). Arctic stratospheric dehydration, that is, the large-scale removal of water vapor from the polar vortex, has been observed infrequently in the Arctic. First spaceborne observations were reported by Pan et al. (2002) based on Improved Limb Atmospheric Spectrometer (ILAS) that measured up to ~3 ppmv water vapor reduction inside the polar vortex. The permanent water vapor removal of ~2 ppmv occurred mostly at altitudes between 23 and 26 km. Pan et al. (2002) also reported some cases when the dehydrated air was observed downwind from mountain wave-induced polar stratospheric clouds (PSCs). Since ILAS, different satellite sensors allowed a continuous monitoring of the stratospheric water vapor distribution (Khosrawi et al., 2018; Lossow et al., 2019). Especially, the remote-sensing observations by the Microwave Limb Sounder (MLS) onboard of the Upper Atmosphere Research Satellite (UARS) and the Earth Observing System (EOS) on Aura (e.g., Herman et al., 2002; Nedoluha et al., 2002) have been used to document Arctic dehydration.

Based on MLS data, Jiménez et al. (2006) reported a widespread dehydration (0.5 ppmv drop in water vapor mixing ratio with respect to the vortex background value) during the exceptionally cold Arctic winter 2004/2005 (Chshyolkova et al., 2007; Manney et al., 2006). Dehydration between 12 and 20 km altitude was observed above the Atlantic, the Norwegian, and the Barents Seas south of Spitsbergen and north of Scandinavia on three consecutive days (25 till 27 January 2005). The time series of the areas of reduced water vapor indicate two separated, coherent regions apparently propagating eastward (Figure 6 in Jiménez et al., 2006). Based on reverse trajectory calculations the authors concluded that the water vapor depletion was due to large-scale condensation inside the cold Arctic vortex.

At first sight the results of Jiménez et al. (2006) seem to be in accordance with the first reported appearance of a stratospheric ice cloud in the long-term record of the German lidar at Ny-Ålesund, Spitsbergen (78.9°N, 11.9°E) on 26 January 2005 (Maturilli & Dörnbrack, 2006). However, Maturilli and Dörnbrack (2006) were able to show that the ice PSC formation and the associated water vapor reduction was most likely due to the adiabatic cooling in the ascending branches of mountain waves locally excited by the flow past Spitsbergen. Another event of mountain wave-induced ice PSCs above Spitsbergen was recently observed by spaceborne lidar measurements (Dörnbrack et al., 2017). The mountain wave-induced ice cloud formation is a decisive process in the Arctic stratosphere. Already, Alexander et al. (2013) pointed at the importance of the downstream effects of major topographical barriers in the Northern Hemisphere. Based on a combination of different satellite sensors and meteorological data, they found that more than 50% of water ice PSCs are due to mountain waves in the Arctic. Especially Greenland's northeast coast is one of the preferred locations of mountain wave-induced PSCs (e.g., Alexander et al., 2013; Pitts et al., 2018).

It turned out that the period end of January 2005, as investigated by Jiménez et al. (2006) and Maturilli and Dörnbrack (2006) also attracted attention by atmospheric dynamicists as the polar vortex was disturbed by planetary waves (Belova et al., 2009; Chshyolkova et al., 2007). Limpasuvan et al. (2007) studied the deep vertical propagation of mountain waves at the east coast of Greenland and their interaction with the Arctic polar vortex. The gravity wave drag associated with breaking mountain waves resulted in a horizontal flow deceleration of up to $120 \text{ m s}^{-1} \text{ day}^{-1}$ suggesting strong interactions between the orographic gravity waves and the polar vortex that resulted in extended areas of depleted horizontal winds downstream of Greenland forming a large-scale gravity wave-induced stratospheric wake.

In addition to the spaceborne observations, there are only a few reports about particular dehydration events based on balloon-borne observations with different types of in situ sensors (e.g., Schiller et al., 2002; Thölix et al., 2016; Vömel et al., 1997) or a combination of different sensors as in situ instrumentation on balloons, high-altitude aircraft, and CALIOP observations (Khaykin et al., 2013). In contrast to the spaceborne limb soundings (providing vertical profiles of the water vapor mixing ratio $q_{\text{H}_2\text{O}}$ with a vertical resolution Δz ranging between 3 and 5 km and covering a horizontal area of up to $200 \times 200 \text{ km}^2$ depending on the viewing geometry), the balloon-borne in situ observations have a fine vertical resolution of $\Delta z \approx 10 \text{ m}$.

As combined and nearly simultaneous in situ observations of stratospheric water vapor profiles and ice PSCs are extremely rare in the Arctic, we briefly communicate unique observations by balloon-borne instruments launched at Sodankylä, Finland (67.37°N, 26.63°E) during the period from 24 till 27 January 2005. The concurrent appearance of both stratospheric ice clouds and significant water vapor reduction points to local dehydration due to ice cloud formation. Additionally, our balloon-borne frost-point hygrometer measured layers of water vapor increase with respect to the climatological mean inside the polar vortex indicating a local rehydration at lower layers. As the physical processes of dehydration and rehydration in relation to the formation of ice PSCs are essentially known, the observations of this particular case confirm former studies. Moreover, they extend our knowledge of the far-ranging impact of mountain waves launched over Greenland on the appearance of ice PSCs over Scandinavia in accordance with the dynamical results of Limpasuvan et al. (2007). We also document the potential of state-of-the-art high-resolution global circulation models (Bauer et al., 2015) to represent the dynamical processes leading to the observed dehydration.

The water vapor as well as the balloon-borne backscatter observations characterizing the stratospheric aerosol particles are presented in section 2. Applying operational European Centre for Medium-Range Weather Forecasts (ECMWF) analyses and state-of-the-art reanalyses ERA5 as described in section 3, we analyze the temperature history of the sampled air mass in order to find possible causes of the observed water vapor

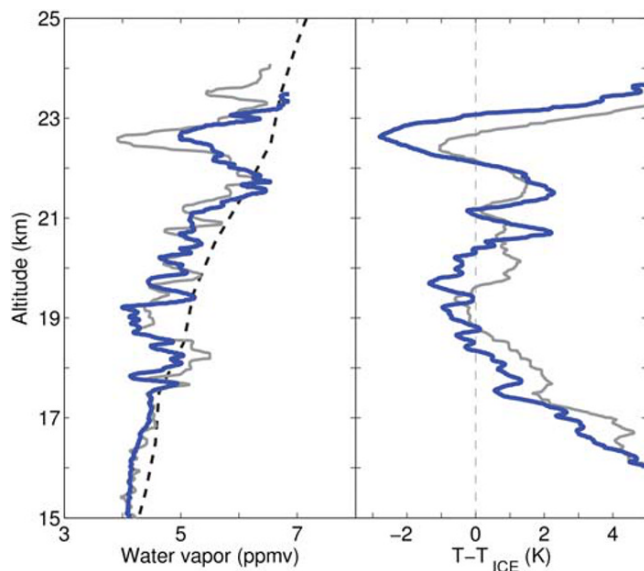


Figure 1. Frostpoint hygrometer $q_{\text{H}_2\text{O}}$ -observations on 26 January 2005 (left panel). Balloon ascent data are shown in blue color and descent data in gray. The balloon was launched at 15:53 UTC. The average water vapor profile in winter 2004/2005 of all inner-vortex soundings is marked by the dashed line. Right panel presents $T - T_{\text{ICE}}$ of the 26 January 2005 sounding using the mean inner-vortex water vapor profile from the winter 2004/2005.

profile (section 4). Section 5 discusses the Sodankylä observations in the context of the complex dynamical processes and concludes the paper.

2. Observations

Water vapor was measured by a balloon-borne frostpoint hygrometer developed by the National Oceanic and Atmospheric Administration/Climate Monitoring and Diagnostics Laboratory (NOAA/CMDL) (Oltmans, 1985; Vömel et al., 1995). This instrument measures the temperature of a cryogenically cooled mirror that maintains a small and constant layer of water ice. Therefore, the mirror temperature equals the frostpoint temperature of the air passing through the sensor. By applying the formula for the saturation water pressure p_{sat} over a plane ice surface the water vapor mixing ratio $q_{\text{H}_2\text{O}}$ can be estimated. The overall accuracy of the instrument is given to be better than 10% (Vömel et al., 1995). Balloon-borne sondes measured the stratospheric aerosol backscatter at wavelengths $\lambda = 490$ and 940 nm, respectively. Their average vertical resolution amounted to $\Delta z = 30$ m (Rosen & Kjöme, 1991). The instrument signal noise was of the order of 1%. The backscatter ratio R_λ is the ratio of total (molecular plus aerosol) to the molecular backscatter. The aerosol color index $\text{CI} = (R_{940} - 1)/(R_{490} - 1)$ allows to distinguish between liquid ($\text{CI} < 6$) and solid ($\text{CI} > 9$) phase particles (Kivi et al., 2001; Larsen et al., 1997). An updated version of the backscatter sonde included a polarization channel that allowed to identify large irregular particles causing significant depolarization. All temperatures reported in this paper were measured by Vaisala RS 80 radiosondes. Their accuracy is ± 0.5 K and the data were recorded every 2 s ($\Delta z \approx 8$ –10 m during the ascent of the balloon).

The frostpoint hygrometer was launched on 26 January 2005 at 15:53 UTC. The balloon burst at an altitude of 26.2 km at 17:36 UTC after drifting about 50.8 km southeast (147.5°) from the launch site at Sodankylä. Both balloon ascent and descent data of $q_{\text{H}_2\text{O}}$ are shown in Figure 1. Between 18.5 km (≈ 60 hPa) and 23.5 km (≈ 25 hPa) altitude, $q_{\text{H}_2\text{O}}$ was reduced by up to 2 ppmv with respect to an average, undisturbed profile calculated from all inner-vortex observations of the winter 2004/2005. Below $z = 18.5$ km, the descent data revealed a light increase of $q_{\text{H}_2\text{O}}$ by 0.5 ppmv in a 1-km-deep layer. Collocated temperature measurements showed that layers of reduced $q_{\text{H}_2\text{O}}$ corresponded to minimum temperature close to or even below T_{ICE} , whereby the strongest cooling was associated with the largest $q_{\text{H}_2\text{O}}$ -depletion near $z \approx 22.5$ km (Figure 1). The ice frostpoint T_{ICE} was calculated according to Murphy and Koop (2005) and by using a mean $q_{\text{H}_2\text{O}}$ profile from inner-vortex observations during the winter 2004/2005. The bulk of the depleted $q_{\text{H}_2\text{O}}$ layer was characterized by strongly fluctuating temperatures close to T_{ICE} . In contrast, the region of increased $q_{\text{H}_2\text{O}}$ was associated with gradually increasing temperatures. The enhanced $q_{\text{H}_2\text{O}}$ values at altitudes in a 1-km-deep layer below 18.5 km suggests rehydration related to the evaporation of sedimenting ice crystals.

The high backscatter values R_λ measured by the sonde launched at 21:06 UTC (i.e., about 3 hr after the $q_{\text{H}_2\text{O}}$ observations) indicates the existence of a PSC covering an unusually deep layer between 16.0 and 25.5 km altitude (Figure 2). In this layer, $R_{940} > 5$ and reaching $R_{940}^{\text{MAX}} \approx 30$ –100 in vertically thin ($\Delta z < 500$ m) layers between 19 and 22 km. Their high backscatter ratios and $\text{CI} > 10$ indicate the presence of ice particles. This interpretation is supported by corresponding layers of $T \leq T_{\text{ICE}}$. It is likely that the remaining part of the PSC layer consisted of solid particles as CI was predominately larger than nine and the temperatures were well below the existence temperature of nitric acid trihydrate (T_{NAT}). This fact is supported by nearly uniform cross-polarization values of 30% at $\lambda = 490$ nm from 16 to 24 km altitude (not shown).

Backscatter observations before and after that event (sondes launched on 24 January at 17:30 UTC and on 27 January at 18:55 UTC, respectively) revealed distinct states of the stratospheric air mass above Sodankylä. The bulk of the PSC observed on 24 January 2005 consisted predominantly of liquid particles ($R_{940} < 5$, $\text{CI} \leq 6$); only the upper and lower edges indicated the presence of solid particles ($\text{CI} \approx 9$), probably NAT as

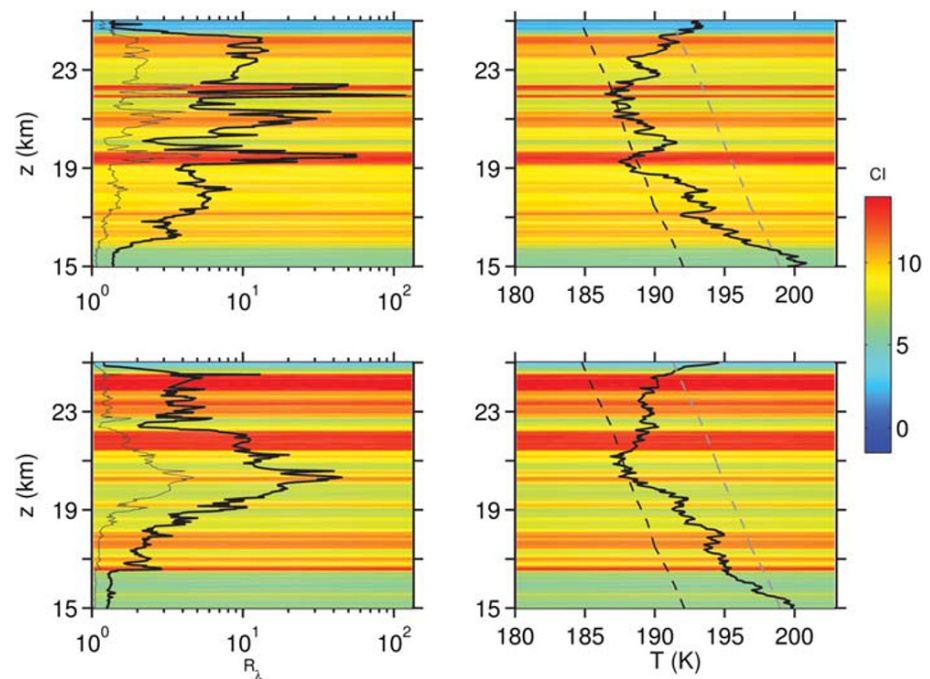


Figure 2. (left) Vertical profiles of aerosol backscatter ratio R_λ on 26 January 2005 at 21:06 UTC (top) and 27 January 2005 at 18:55 UTC (bottom) measured by balloon-borne backscatter sondes. Thick solid lines mark $\lambda = 940$ nm, thin lines $\lambda = 490$ nm. (right) Corresponding temperature profiles. The threshold temperatures T_{ICE} and T_{NAT} are indicated by thin black and gray dashed lines, respectively. They are calculated assuming mean inner-vortex volume mixing ratios of water vapor and a LIMS profile at 68°N for HNO_3 . The aerosol color index $CI = (R_{940} - 1)/(R_{490} - 1)$ is shown as color shading in the background of each plot.

$T < T_{NAT}$. However, the large R_λ values on 27 January 2005 resembles the ones observed one day before, that is, the PSC consisted mainly of solid particles (Figure 2). The ice particles with $R_{940} > 10$ were confined in a single layer between 19 and 21 km altitude which corresponds to $T \approx T_{ICE}$ and $CI > 9$. Comparing these observations with the water vapor and backscatter observations of 26 January 2006, we see the strongest reduction in water vapor occurring above $z = 22$ km. Although $R_{940} \approx 10$, $T > T_{ICE}$ does not allow the existence of ice particles. Ice particle layers were predominantly observed at lower altitudes corresponding to layers of $T < T_{ICE}$. Here water vapor was reduced in the mean by 0.5 ppmv for the 19 to 21 km layer. This region obeyed properties of a quasi-homogeneous mixed layer with fluctuating components of R_{940} , $q_{\text{H}_2\text{O}}$, and CI . In section 4 we place the observation into a meteorological context.

3. Numerical Weather Prediction Model Data

Three different products of the integrated forecast system (IFS) of the ECMWF provide meteorological data to characterize the atmospheric situation. The operational analyses of the deterministic high-resolution (HRES) IFS cycle Cy28r1 have a horizontal resolution of about 40 km (T_{L511}) and 60 vertical levels. The model top is located at 0.1 hPa. In addition to the operational analysis we consider two reanalyses. The data assimilation system used to produce ERA-Interim is based on a 2006 release of the IFS (Cy31r2). The spatial resolution of the data set is ≈ 80 km (T_{L255} spectral) on 60 levels in the vertical from the surface up to 0.1 hPa (Dee et al., 2011). The more recent reanalysis ERA5 have been produced by IFS cycle Cy41r2 (Hersbach et al., 2020). The enhanced horizontal resolution of 31 km globally was achieved by changing from linear (T_L) to cubic (T_{CO}) spectral truncation and introducing an octahedral reduced Gaussian grid. With the cubic spectral truncation the shortest resolved wave is represented by four rather than two grid points and the octahedral grid is globally more uniform than the previously used reduced Gaussian grid (Malardel & Wedi, 2016). The model top is at 0.01 hPa and 137 vertical hybrid levels are used. Here we use the updated

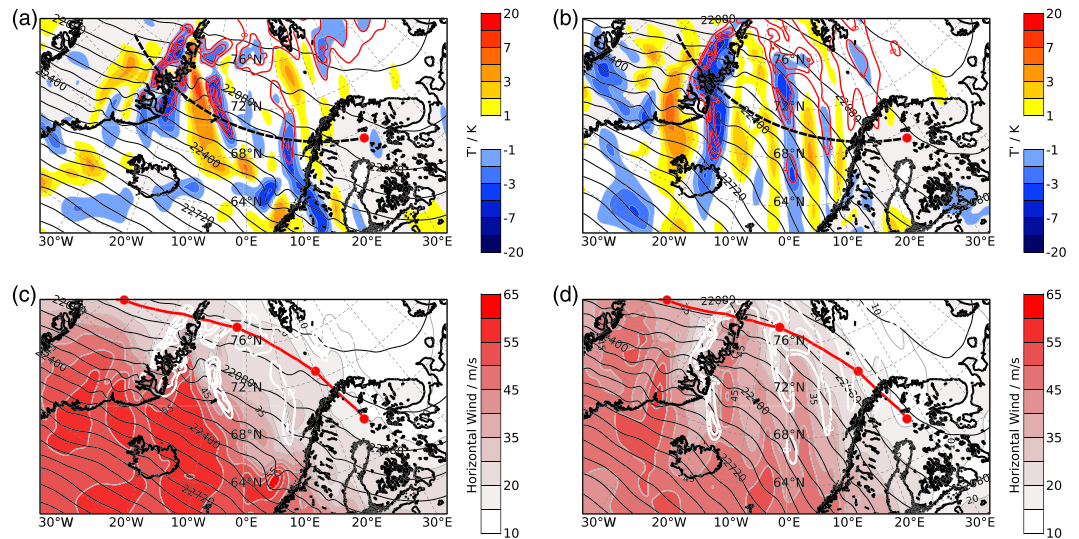


Figure 3. (a, b) ERA5 temperature perturbations T' (K, color shaded) at 30 hPa on 25 and 26 January 2005 18 UTC. (c, d) Horizontal wind (m s^{-1} , color shaded) at 30 hPa and the same times as in panels (a) and (b). In all panels, geopotential height (m, increment 80 m, black solid lines) and $T - T_{\text{ICE}} \leq 0$ (red or white solid lines, interval 1 K). The red and white encircled areas are regions where ice clouds are likely to exist. The bold dashed black line marks the baseline of the vertical sections shown in Figure 4. The red dot marks the position of Sodankylä, Finland. In panels (c) and (d), a backward trajectory starting at 67°N and 27°E is added, the dots are set at every 12 hr from the start time at 18 UTC on 26 January 2005.

and modified version ERA5.1 as Simmons et al. (2020) showed an improved representation of stratospheric temperature fields for the years 2000 to 2006.

In the spirit of Dörnbrack et al. (2017), temperature perturbations T' are calculated as the difference between the temperature field retrieved at full spectral resolution and the spectrally truncated fields T_{CO106} (Malardel & Wedi, 2016; Wedi, 2014); the total horizontal wave number 106 is selected as it can be used to separate large-scale synoptic processes from inertia gravity waves (Schumann, 2019; Žagar et al., 2017).

4. Meteorological Analysis

Figure 3 displays the magnitude of the horizontal wind V_H and the temperature perturbations T' related to mesoscale gravity waves resolved by the ERA5 data. For both times, the plots reveal alternating and successive T' minima and maxima extending from the east coast of Greenland to Scandinavia. The phase lines of these wave-induced temperature anomalies are nearly perpendicular to the contour lines of the geopotential height Z and extend downstream as well as southeast over the Atlantic. This meridional phase propagation is related to the horizontal dispersion of the quasi-steady hydrostatic mountain waves (Gill, 1982; Smith, 1989) excited during this period (Limpasuvan et al., 2007). Here the gravity waves propagate both downstream and meridionally into the core of the polar night jet (PNJ) that is located to the south over the Atlantic (marked by denser contour lines of Z and deeper tinting for V_H). The long-lasting flow over Greenland excited inertia-gravity waves with horizontally long modes ($\lambda > 500$ km) propagating into the direction of the ambient wind, a process similar to that observed in the lee of the Scandinavian mountains (Dörnbrack et al., 1999, 2002). The additional meridional propagation into the PNJ is a dynamical process well-described by Sato et al. (2012) and further discussed by Ehard et al. (2017) and Jiang et al. (2019) for the Southern Hemisphere.

Figure 4 displays vertical sections along the baseline sketched in Figure 3 for the 25 January 2005 18 UTC (i.e., 24 hr before our $q_{\text{H}_2\text{O}}$ observation) and 26 January 2005 18 UTC. It reveals that the vertical propagation leads to enhanced T' amplitudes in the stratosphere attaining more than 10 K. Both panels illustrate the far-ranging impact of horizontal gravity wave propagation clearly. Both in Figures 3 and 4, the difference $T - T_{\text{ICE}} \leq 0$ is plotted in addition to T' . It turns out that the lower stratosphere at about 20 to 50 hPa is

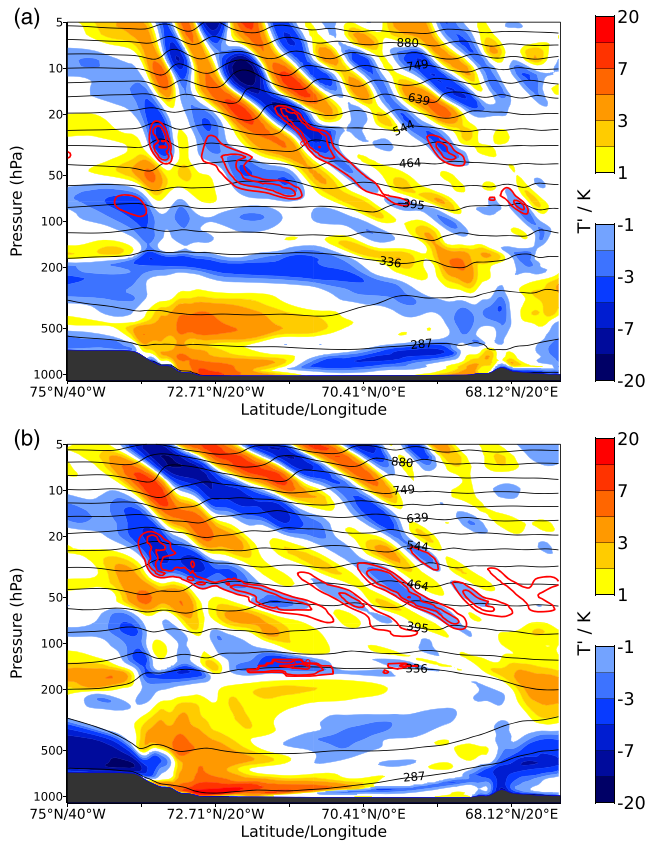


Figure 4. ERA5 temperature perturbations T' (K, color shaded) above the baseline shown in Figure 3 on 25 and 26 January 2005 18 UTC (a, b). Potential temperature (K, solid black lines) and $T - T_{ICE} \leq 0$ are shown (red solid lines, interval 1 K). T_{ICE} is calculated using the ERA5 water vapor values and the red encircled areas are regions where ice clouds are likely to exist; the altitude range of interest in this study is between 100 and 20 hPa.

populated with regions where polar stratospheric ice clouds can exist in the ascending cold branches of the horizontally propagating mountain waves. Both panels in Figure 4 also manifest that the Atlantic-crossing gravity wave propagation is sustained for a long time period. This finding is in accordance with the numerical results by Limpasuvan et al. (2007) showing the deceleration of the PNJ by stratospheric mountain waves from the flow past Greenland.

Figures 5 and 6 complement the presentation of the meteorological situation by displaying the temperature perturbations T' for three different data sets: ERA5, ERA interim, and the operational ECMWF analyses. All ECMWF data sets consistently simulate the gravity wave propagation across the Atlantic. However, the largest T' amplitudes are produced by the ERA5 data. Due to the lesser horizontal resolution, the ERA Interim data generate weaker amplitudes and horizontally longer waves, the operational analyses and the ERA5 produce nearly similar results (Figure 5). All analyses show $q_{H_2O}^{ECMWF}$ values close to 4.5 ppmv at 30 hPa. Compared to the observed values of $q_{H_2O} \approx 6$ ppmv, this is an underestimate by 1.5 ppmv. A similar deviation was found during an international hygrometer intercomparison as discussed by Maturilli and Dörnbrack (2006). Therefore, we increased the q_{H_2O} values by 1.5 ppmv in order to fit the anticipated background value of q_{H_2O} . The modified T_{ICE} values are used for Figure 6 and overall they produce larger regions where polar stratospheric ice clouds can exist compared to the Figure 5. The comparison of Figures 5a with 6c reveals the impact of the better resolved ERA5 data compared to the operational analyses even by using larger q_{H_2O} values for the latter. The spatial distribution of $T - T_{ICE}$ regions is similar in both panels. In the ERA5 plot, however, the more pronounced occurrence of ice PSCs is caused by the larger mountain wave-induced temperature perturbations producing lower local T values. In contrast, the larger $T - T_{ICE}$ area in the operational analysis (compared to Figure 5c) is solely due to the modified and enhanced water vapor mixing ratio.

The temperature history of the sampled air mass is explored by means of backward trajectories that were launched in a box between 26°E and 30°E and 65°N and 67°N on 26 January 2005 at 18 UTC. The applied trajectory scheme LAGRANTO (Sprenger & Wernli, 2015; Wernli & Davies, 1997) was run with three different meteorological data sets: the T_1 511/L60 operational ECMWF analyses interpolated on a regular $0.5^\circ \times 0.5^\circ$ latitude-longitude grid every 6 hr, the ERA Interim, and the ERA5 data at 3 hr resolution. Figure 7 depicts the temporal evolution of the air parcels temperature difference $T - T_{ICE}$ from ERA5, whereby T_{ICE} was calculated by assuming water vapor values $q_{H_2O}^{ERA5} + 1.5$ ppmv. At 30 hPa, initial $q_{H_2O}^{ERA5}$ values belonging to the start area above northern Scandinavia were about 4.5 ppmv at 30 hPa and 3.2 ppmv at 50 hPa. As discussed for Figure 6, we added a constant value of 1.5 ppmv to the actual ERA5 data.

All parcels passed (following their trajectories backward in time) the North Atlantic westward and crossed Greenland's east coast at about 74°N to 78°N (Figures 3c and 3d). The temperature T of a good portion of the air parcels released both at 30 and 50 hPa remained or dropped below T_{ICE} during the first 30–36 hr. However, the most prominent cooling of the air parcels by about 8 K (at 30 hPa) and 11 K (at 50 hPa) occurred between 60 and 36 hr prior to the observation. Inspection of the pressure change along the trajectories suggests that this cooling was caused by large-scale adiabatic lifting of stratospheric air parcels by the high tropopause of a high-pressure system. The air parcels passed Greenland's east coast between –24 and –36 hr. There, $T - T_{ICE}$ values along the different trajectories had their largest spread due to the wave-induced temperature fluctuations in the mountain waves. This statement becomes evident if one compares the solid lines in Figure 7 with the dashed ones that represent the temporal evolution of air parcels

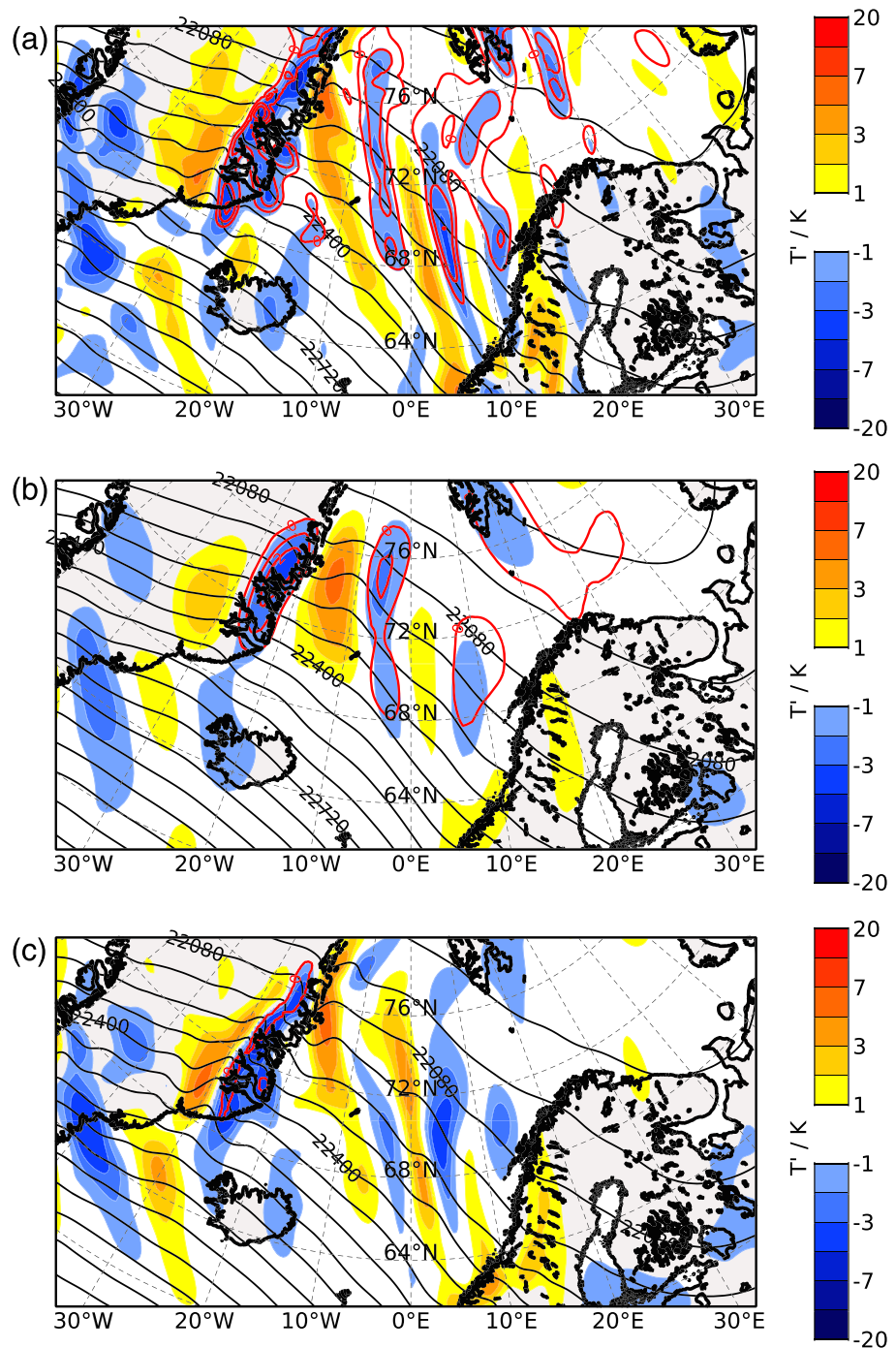


Figure 5. Temperature perturbations T' (K, color shaded) at 30 hPa on 26 January 2005 06 UTC from ERA5 (a), ERA Interim (b), and the operational ECMWF T511/L60 analyses (c). Same layout as in Figure 3a. T_{ICE} is calculated using the ECMWF water vapor values, and the red encircled areas are regions where ice clouds are likely to exist.

under the large-scale background conditions. Both curves deviate only slightly during the cooling above the anticyclone. However, in the lee of Greenland (for times larger than -36 hr) gravity wave-induced temperature perturbations dominated and led to episodes of localized cooling. Trajectories calculated by using the other meteorological data show qualitatively similar results to the fully resolved ERA5 results, however, the mountain wave-induced temperature perturbations are much smaller and the ensemble of trajectory curves spreads less and stays closer to the dashed lines in Figure 7.

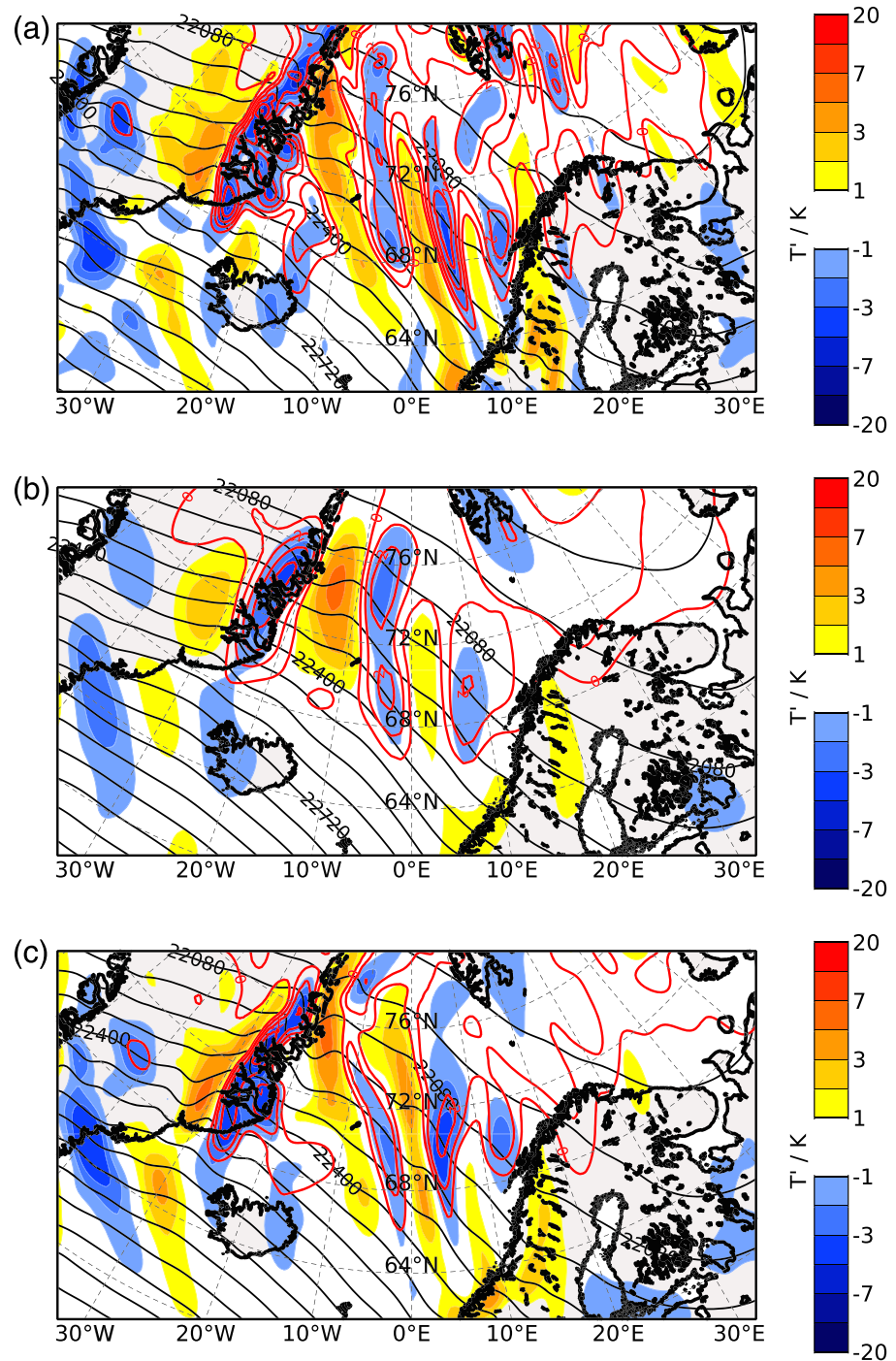


Figure 6. Temperature perturbations T' (K, color shaded) at 30 hPa on 26 January 2005 06 UTC from ERA5 (a), ERA Interim (b), and the operational ECMWF T511/L60 analyses (c). Same layout as in Figure 5, however, T_{ICE} values are calculated by adding 1.5 ppmv water vapor to the actual ECMWF data.

In order to investigate whether homogeneous freezing was responsible for the PSC formation, we calculated the ice saturation ratio $S_i = p_w/p_{sat}(T)$, where p_w is the partial pressure of water vapor and p_{sat} is the saturation vapor pressure over a plane ice surface, calculated after Murphy and Koop (2005), along the backward trajectories. Sensitivity tests with formulas provided by Sonntag (1990) and Marti and Mauersberger (1993) revealed that the results are not sensitive to the choice of the $p_{sat}(T)$ formula in our case. Furthermore, the

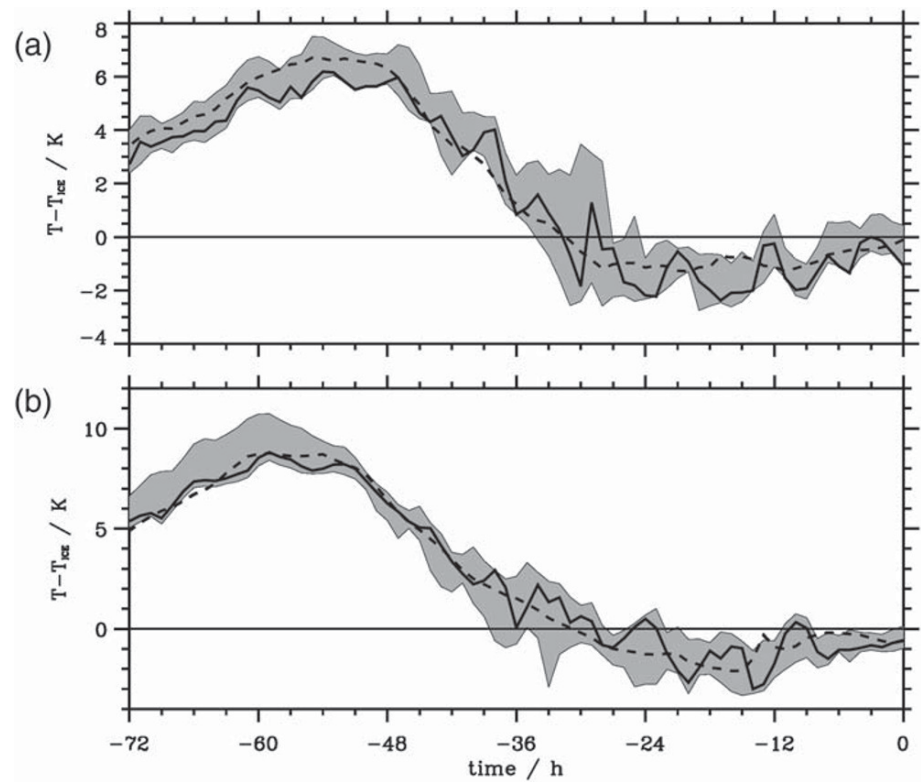


Figure 7. $T - T_{ICE}$ along the ERA5-based trajectory launched at 67°N and 27°E in the vicinity of the Sodankylä sounding station and at 30 hPa (a) and 50 hPa (b) on 26 January 2005 at 18 UTC (black solid line). The shaded area marks the minima and maxima of $T - T_{ICE}$ of 15 trajectories released in the area between 26°E and 30°E and 65°N and 67°N at each pressure level. The dashed line displays the temporal evolution along the trajectory launched at 67°N and 27°E , however, calculated with LAGRANTO input data retrieved at reduced spectral resolution ERA5 data, characterizing the large-scale background fields without gravity waves.

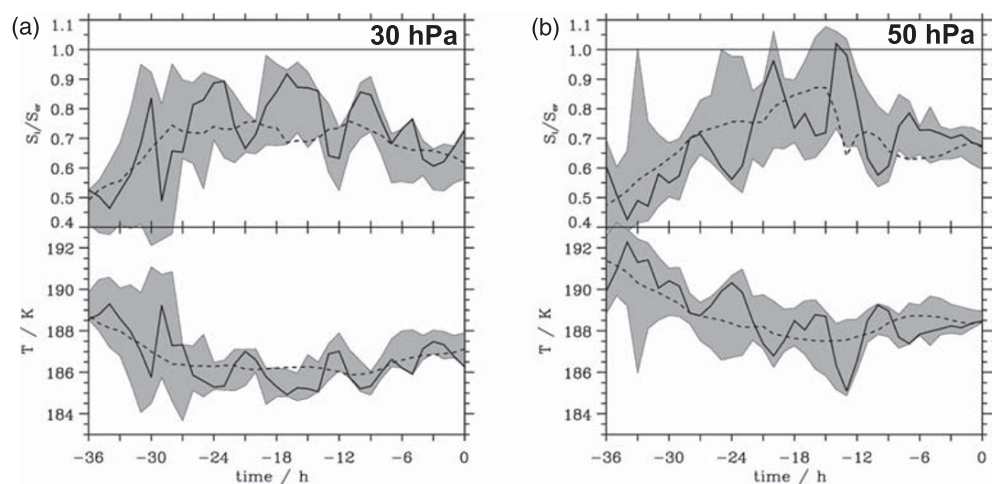


Figure 8. Ratio of the ice saturation ratio S_i to the threshold value S_{cr} where homogeneous nucleation occurs and temperature (K) along a backward trajectory released at 67°N and 27°E in the vicinity of the Sodankylä sounding station on 26 January 2005 at 18 UTC (black solid line). The shaded area marks the minima and maxima T values of 15 trajectories released in the area between 26°E and 30°E and 65°N and 67°N at each of the departure levels at 30 hPa (a) and 50 hPa (b). The dashed line displays the temporal evolution along the trajectory launched at 67°N and 27°E , however, calculated with reduced spectral resolution ERA5 data, characterizing the large-scale background fields without gravity waves.

freezing threshold saturation ratio S_{cr} for homogeneous nucleation of ice crystals from supercooled aqueous solution droplets (Koop et al., 2000) was computed using the approximation by Kärcher and Lohmann (2002). Generally, in the temperature range between 184 and 190 K, S_{cr} is nearly constant and amounts to about 1.7; that is, homogeneous freezing requires large ice supersaturation.

Figure 8 depicts the ratio S_i/S_{cr} for all backward trajectories during the last 36 hr. The ERA5 temperature increases from around 186 K at 30 hPa (~ 22 km) and 188 K at 50 hPa (~ 19 km) to values above 190 K for $t = -36$ hr. Although S_i is larger than 1, the ice saturation ratio S_i rarely exceeds the threshold S_{cr} . S_i/S_{cr} is maximum near the east coast of Greenland and levels at about 0.6–0.7 over Scandinavia. The largest spread of S_i/S_{cr} values for all trajectories occurred above and in the lee of Greenland. These strong fluctuations were caused by mountain wave-induced stratospheric temperature anomalies resolved by the ERA5 data.

5. Discussion and Conclusions

We reported on unique balloon-borne stratospheric observations of water vapor and aerosol backscatter in the Arctic winter 2004/2005. Antarctic-like water vapor dehydration and rehydration and solid ice particles could be detected by the frostpoint hygrometer and the backscatter sondes during a 3-day period from 24 to 27 January 2005. Combined high-resolution measurements as those presented in this paper have only been conducted in rare intervals and they constitute a reliable means to investigate the dynamical conditions under which the observations were made.

The observed magnitude of dehydration was similar to the maximum value of 1.6 ppmv as reported by Khaykin et al. (2013) for another January case. We found the largest amplitude of dehydration being centered to layer 22.2–23 km. Thus, our in situ water vapor observation was above the altitude reported by Jiménez et al. (2006), who found 0.5 ppmv water vapor reduction in the layer between 12 and 20 km based on the MLS data for the same period. Vömel et al. (1997) measured even lower water vapor mixing ratios of about 2.4 ppmv at similar altitudes in January 1996. However, they did not observe rehydration below the strongly dehydrated layer. Observed backscatter ratios and CI in the ice PSC were similar to the previous studies, for example, by Kivi et al. (2001). Pitts et al. (2018) analyzed the frequency of Arctic ice PSC observations at 21 km from 11 Arctic winters as a function of $T - T_{ICE}$. The observed majority of the Arctic ice PSC have been observed while $T - T_{ICE}$ was between 0 and -2 K (Pitts et al., 2018). This finding is in agreement with our in situ observations.

The ice PSCs were predominantly formed above Greenland's east coast and over the Northern Atlantic by the adiabatic cooling in the ascending branches of mountain waves. As the mountain waves were excited during a period lasting about 3 days, these essentially mesoscale inertia-gravity waves propagated both vertically as well as zonally and meridionally and generated a large and persistent gravity wave-induced stratospheric wake downstream of Greenland. Considering the same period, Limpasuvan et al. (2007) found a considerable momentum reduction at stratospheric levels. In this dynamically produced wake also the formation and existence conditions of PSCs were strongly modified and wave-induced cooling was able to bring the local temperatures at least 3 to 4 K below the frostpoint T_{ICE} . Based on laboratory experiments, Koop et al. (2000) could show that this condition is required for homogeneous ice nucleation.

Here the most recent meteorological ECMWF reanalyses ERA5 are applied to interpret the series of balloon-borne water vapor and backscatter observations over northern Scandinavia. Stratospheric temperature fluctuations due to the inertia-gravity waves over the Atlantic caused additional localized cooling and generated regions of $T < T_{ICE}$ (Figures 3 and 4). As a result, the observed air mass above Sodankylä was composed of solid aerosols with remnants of the ice layer formed over Greenland. This far-ranging influence of mountain waves excited at the east coast of Greenland on the observations over Scandinavia is a new finding previously not published in the literature.

Moreover, due to the presence of a tropospheric anticyclone between Greenland and Scandinavia (Maturilli & Dörnbrack, 2006) the tropopause as well as the isentropes in the lower stratosphere were lifted. Similar meteorological situations were met in the studies by Vömel et al. (1997) and Teitelbaum and Sadourny (1998). Thus, the ice particles approximately maintained their temperature or warmed only slightly while propagating toward Scandinavia (see Figure 7). The fact that the temperature in

Greenland's wake was below T_{ICE} for a significant amount of time is important and may be a key ingredient for the extensive dehydration. Additionally, during this period ice particles were able to sediment out and reach warmer layers where they could evaporate and rehydrate a lower layer.

Recent investigations of the stratospheric flow and temperature field above Greenland (Doyle et al., 2005; Leutbecher & Volkert, 2000; Limpasuvan et al., 2007; Ólafsson & Ágústsson, 2009), Scandinavia (Wagner et al., 2017) and New Zealand (Smith & Kruse, 2017) indicate that a broad spectrum of mountain waves exists in the lower stratosphere and can be numerically resolved by using finer spatial resolutions. Especially, the fast vertically propagating hydrostatic or nonhydrostatic gravity waves can lower the stratospheric temperatures by up to 10 K (see also Maturilli & Dörnbrack, 2006). These gravity waves with horizontal wavelengths of about 20 km cannot be resolved in ERA5. Their additional contribution might have brought the local temperatures above Greenland's east coast well below $T_{ICE} - 4$ K and eventually led to conditions $S_i/S_{cr} > 1$, large enough for homogeneous ice formation. However, the ability of the most recent reanalysis ERA5 to resolve stratospheric mountain waves directly above the source and far downstream of it indicates a significant trend that the finer resolution and increasing realism of model outputs offers a valuable quantitative source for mesoscale flow components, which were hitherto not accessible globally (Bauer et al., 2015; Dörnbrack et al., 2017).

Data Availability Statement

Observational data used in this study are archived in the Network for the Detection of Atmospheric Composition Change (NDACC) data repository (<ftp://ftp.cpc.ncep.noaa.gov/ndacc>). The ERA-Interim and the ERA5 data can be retrieved from the following web sites (<https://www.ecmwf.int/en/forecasts/datasets/reanalysis-datasets/era-interim> and from <https://confluence.ecmwf.int/display/CKB/How+to+download+ERA5>). The most recent ERA5.1 data are available via the Copernicus Climate Change Service (<https://confluence.ecmwf.int/display/CKB/How+to+download+ERA5#HowtodownloadERA5-StepC:DownloadERA5dataNOTlistedinCDSthroughCDSAPI>).

Acknowledgments

This work was supported by the EU through the research projects SCOUT-O3 and GAIA-CLIM and by the Academy of Finland through the UTLs project (Grant 140408). We are grateful to James Rosen and Norman Kjöme for their support to the aerosol backscatter sonde measurements. The FMI staff is acknowledged for their effort in the sonde campaign in Sodankylä. Part of this research was conducted within the scope of the German research initiative Role of the Middle Atmosphere in Climate (ROMIC) under Grant 01LG1206A by the German Ministry for Education and Research. Partial funding was also provided by the German Science Foundation (DFG) via the research unit MS-GWaves (GW-TP/DO 1020/9-1 and PACOG/RA 1400/6-1).

References

- Alexander, S. P., Klekociuk, A. R., McDonald, A. J., & Pitts, M. C. (2013). Quantifying the role of orographic gravity waves on polar stratospheric cloud occurrence in the Antarctic and the Arctic. *Journal of Geophysical Research: Atmospheres*, 118, 11,493–11,507. <https://doi.org/10.1002/2013JD020122>
- Bauer, P., Thorpe, A., & Brunet, G. (2015). The quiet revolution of numerical weather prediction. *Nature*, 525, 47–55. <https://doi.org/10.1038/nature14956>
- Belova, A., Kirkwood, S., & Murtagh, D. (2009). Planetary waves in ozone and temperature in the Northern Hemisphere winters of 2002/2003 and early 2005. *Annales Geophysicae*, 27(3), 1189–1206. <https://doi.org/10.5194/angeo-27-1189-2009>
- Chshyolkova, T., Manson, A. H., Meek, C. E., Aso, T., Avery, S. K., Hall, C. M., et al. (2007). Polar vortex evolution during Northern Hemispheric winter 2004/05. *Annales Geophysicae*, 25(6), 1279–1298. <https://doi.org/10.5194/angeo-25-1279-2007>
- Dee, D. P., Uppala, S. M., Simmons, A. J., Berrisford, P., Poli, P., Kobayashi, S., et al. (2011). The ERA-Interim reanalysis: Configuration and performance of the data assimilation system. *Quarterly Journal of the Royal Meteorological Society*, 137(656), 553–597. <https://doi.org/10.1002/qj.828>
- Dörnbrack, A., Birner, T., Fix, A., Flentje, H., Meister, A., Schmid, H., et al. (2002). Evidence for inertia gravity waves forming polar stratospheric clouds over Scandinavia. *Journal of Geophysical Research*, 107(D20), 8287. <https://doi.org/10.1029/2001JD000452>
- Dörnbrack, A., Gisinger, S., Pitts, M. C., Poole, L. R., & Maturilli, M. (2017). Multilevel cloud structures over Svalbard. *Monthly Weather Review*, 145(4), 1149–1159. <https://doi.org/10.1175/MWR-D-16-0214.1>
- Dörnbrack, A., Leutbecher, M., Kivi, R., & Kyrö, E. (1999). Mountain-wave-induced record low stratospheric temperatures above Northern Scandinavia. *Tellus A*, 51(5), 951–963. <https://doi.org/10.1034/j.1600-0870.1999.00028.x>
- Doyle, J. D., Shapiro, M. A., Jiang, Q., & Bartels, D. L. (2005). Large-amplitude mountain wave breaking over Greenland. *Journal of the Atmospheric Sciences*, 62(9), 3106–3126. <https://doi.org/10.1175/JAS3528.1>
- Ehard, B., Kaifler, B., Dörnbrack, A., Preusse, P., Eckermann, S. D., Bramberger, M., et al. (2017). Horizontal propagation of large-amplitude mountain waves into the polar night jet. *Journal of Geophysical Research: Atmospheres*, 122, 1423–1436. <https://doi.org/10.1002/2016JD025621>
- Forster, P. M. F., & Shine, K. P. (1999). Stratospheric water vapour changes as a possible contributor to observed stratospheric cooling. *Geophysical Research Letters*, 26(21), 3309–3312. <https://doi.org/10.1029/1999GL010487>
- Forster, P. M. F., & Shine, K. P. (2002). Assessing the climate impact of trends in stratospheric water vapor. *Geophysical Research Letters*, 29(6), 10-1–10-4. <https://doi.org/10.1029/2001GL013909>
- Gill, A. E. (1982). *Atmosphere-Ocean Dynamics* (Vol. 30, 1st ed., pp. 1–681). New York: Academic Press. Paperback ISBN: 9780122835223, eBook ISBN: 9780080570525
- Herman, R. L., Drdla, K., Spackman, J. R., Hurst, D. F., Popp, P. J., Webster, C. R., et al. (2002). Hydration, dehydration, and the total hydrogen budget of the 1999/2000 winter Arctic stratosphere. *Journal of Geophysical Research*, 107(D5), 8320. <https://doi.org/10.1029/2001JD001257>
- Hersbach, H., Bell, B., Berrisford, P., Hirahara, S., Horányi, A., Muñoz-Sabater, J., et al. (2020). The ERA5 global reanalysis. *Quarterly Journal of the Royal Meteorological Society*, 146(730), 1999–2049. <https://doi.org/10.1002/qj.3803>

- Jiang, Q., Doyle, J. D., Eckermann, S. D., & Williams, B. P. (2019). Stratospheric trailing gravity waves from New Zealand. *Journal of the Atmospheric Sciences*, 76(6), 1565–1586. <https://doi.org/10.1175/JAS-D-18-0290.1>
- Jiménez, C., Pumphrey, H. C., MacKenzie, I. A., Manney, G. L., Santee, M. L., Schwartz, M. J., et al. (2006). EOS MLS observations of dehydration in the 2004–2005 polar winters. *Geophysical Research Letters*, 33, L16806. <https://doi.org/10.1029/2006GL025926>
- Kärcher, B., & Lohmann, U. (2002). A parameterization of cirrus cloud formation: Homogeneous freezing of supercooled aerosols. *Journal of Geophysical Research*, 107(D2), AAC 4-1–AAC 4-10. <https://doi.org/10.1029/2001JD000470>
- Khaykin, S. M., Engel, I., Vömel, H., Formanyuk, I. M., Kivi, R., Korshunov, L. I., et al. (2013). Arctic stratospheric dehydration—Part 1: Unprecedented observation of vertical redistribution of water. *Atmospheric Chemistry and Physics*, 13(22), 11,503–11,517. <https://doi.org/10.5194/acp-13-11503-2013>
- Khosrawi, F., Lossow, S., Stiller, G. P., Rosenlof, K. H., Urban, J., Burrows, J. P., et al. (2018). The SPARC water vapour assessment II: Comparison of stratospheric and lower mesospheric water vapour time series observed from satellites. *Atmospheric Measurement Techniques*, 11(7), 4435–4463. <https://doi.org/10.5194/amt-11-4435-2018>
- Kivi, R., Kyrö, E., Dörnbrack, A., & Birner, T. (2001). Observations of vertically thick polar stratospheric clouds and record low temperature in the Arctic vortex. *Geophysical Research Letters*, 28(19), 3661–3664. <https://doi.org/10.1029/2001GL013187>
- Koop, T., Luo, B., Tsias, A., & Peter, T. (2000). Water activity as the determinant for homogeneous ice nucleation in aqueous solutions. *Nature*, 406, 611–614. <https://doi.org/10.1038/35020537>
- Larsen, N., Knudsen, B. M., Rosen, J. M., Kjöme, N. T., Neuber, R., & Kyrö, E. (1997). Temperature histories in liquid and solid polar stratospheric cloud formation. *Journal of Geophysical Research*, 102(D19), 23,505–23,517. <https://doi.org/10.1029/97JD01666>
- Leutbecher, M., & Volkert, H. (2000). The propagation of mountain waves into the stratosphere: Quantitative evaluation of three-dimensional simulations. *Journal of the Atmospheric Sciences*, 57(18), 3090–3108. [https://doi.org/10.1175/1520-0469\(2000\)057<3090:TPOMWI>2.0.CO;2](https://doi.org/10.1175/1520-0469(2000)057<3090:TPOMWI>2.0.CO;2)
- Limpasuvan, V., Wu, D. L., Joan Alexander, M., Xue, M., Hu, M., Pawson, S., & Perkins, J. R. (2007). Stratospheric gravity wave simulation over Greenland during 24 January 2005. *Journal of Geophysical Research*, 112, D10115. <https://doi.org/10.1029/2006JD007823>
- Lossow, S., Khosrawi, F., Kiefer, M., Walker, K. A., Bertaux, J.-L., Blanot, L., et al. (2019). The SPARC water vapour assessment II: Profile-to-profile comparisons of stratospheric and lower mesospheric water vapour data sets obtained from satellites. *Atmospheric Measurement Techniques*, 12(5), 2693–2732. <https://doi.org/10.5194/amt-12-2693-2019>
- Malardel, S., & Wedi, N. P. (2016). How does subgrid-scale parametrization influence nonlinear spectral energy fluxes in global NWP models? *Journal of Geophysical Research: Atmospheres*, 121, 5395–5410. <https://doi.org/10.1002/2015JD023970>
- Manney, G. L., Santee, M. L., Froidevaux, L., Hoppel, K., Livesey, N. J., & Waters, J. W. (2006). EOS MLS observations of ozone loss in the 2004–2005 Arctic winter. *Geophysical Research Letters*, 33, L04802. <https://doi.org/10.1029/2005GL024494>
- Marti, J., & Mauersberger, K. (1993). A survey and new measurements of ice vapor pressure at temperatures between 170 and 250 K. *Geophysical Research Letters*, 20(5), 363–366. <https://doi.org/10.1029/93GL00105>
- Maturilli, M., & Dörnbrack, A. (2006). Polar stratospheric ice cloud above Spitsbergen. *Journal of Geophysical Research*, 111, D18210. <https://doi.org/10.1029/2005JD006967>
- Maycock, A. C., Joshi, M. M., Shine, K. P., Davis, S. M., & Rosenlof, K. H. (2014). The potential impact of changes in lower stratospheric water vapour on stratospheric temperatures over the past 30 years. *Quarterly Journal of the Royal Meteorological Society*, 140(684), 2176–2185. <https://doi.org/10.1002/qj.2287>
- Maycock, A. C., Joshi, M. M., Shine, K. P., & Scaife, A. A. (2013). The circulation response to idealized changes in stratospheric water vapor. *Journal of Climate*, 26(2), 545–561. <https://doi.org/10.1175/JCLI-D-12-00155.1>
- Murphy, D. M., & Koop, T. (2005). Review of the vapour pressures of ice and supercooled water for atmospheric applications. *Quarterly Journal of the Royal Meteorological Society*, 131(608), 1539–1565. <https://doi.org/10.1256/qj.04.94>
- Nedoluha, G. E., Bevilacqua, R. M., & Hoppel, K. W. (2002). POAM III measurements of dehydration in the Antarctic and comparisons with the Arctic. *Journal of Geophysical Research*, 107(D20), 8290. <https://doi.org/10.1029/2001JD001184>
- Ólafsson, H., & Ágústsson, H. (2009). Gravity wave breaking in easterly flow over Greenland and associated low level barrier and reverse tip-jets. *Meteorology and Atmospheric Physics*, 104(9), 191–197. <https://doi.org/10.1007/s00703-009-0024-9>
- Oltmans, S. J. (1985). Measurements of water vapor in the stratosphere with a frost point hygrometer. In *International symposium on moisture and humidity* (pp. 251–258). Washington, DC: Instrument Society of America.
- Pan, L. L., Randel, W. J., Nakajima, H., Massie, S. T., Kanzawa, H., Sasano, Y., et al. (2002). Satellite observation of dehydration in the Arctic polar stratosphere. *Geophysical Research Letters*, 29(8), 25-1–25-4. <https://doi.org/10.1029/2001GL014147>
- Pitts, M. C., Poole, L. R., & Gonzalez, R. (2018). Polar stratospheric cloud climatology based on CALIPSO spaceborne lidar measurements from 2006 to 2017. *Atmospheric Chemistry and Physics*, 18(15), 10,881–10,913. <https://doi.org/10.5194/acp-18-10881-2018>
- Rosen, J. M., & Kjöme, N. T. (1991). Backscattersonde: A new instrument for atmospheric aerosol research. *Applied Optics*, 30(12), 1552–1561. <https://doi.org/10.1364/AO.30.001552>
- Sato, K., Tateno, S., Watanabe, S., & Kawatani, Y. (2012). Gravity wave characteristics in the southern hemisphere revealed by a high-resolution middle-atmosphere general circulation model. *Journal of the Atmospheric Sciences*, 69(4), 1378–1396. <https://doi.org/10.1175/JAS-D-11-0101.1>
- Schiller, C., Bauer, R., Cairo, F., Deshler, T., Dörnbrack, A., Elkins, J., et al. (2002). Dehydration in the Arctic stratosphere during the SOLVE/THESEO-2000 campaigns. *Journal of Geophysical Research*, 107(D20), 8293. <https://doi.org/10.1029/2001JD000463>
- Schumann, U. (2019). The horizontal spectrum of vertical velocities near the tropopause from global to gravity wave scales. *Journal of the Atmospheric Sciences*, 76(12), 3847–3862. <https://doi.org/10.1175/JAS-D-19-0160.1>
- Simmons, A., Soci, C., Nicolas, J., Bell, B., Berrisford, P., Dragani, R., et al. (2020). Global stratospheric temperature bias and other stratospheric aspects of ERA5 and ERA5.1. *ECMWF Technical Memorandum*, 859. <https://doi.org/10.21957/rcxqfmg0>
- Smith, R. B. (1989). Hydrostatic airflow over mountains. *Advances in Geophysics*, 31, 1–41. [https://doi.org/10.1016/S0065-2687\(08\)60052-7](https://doi.org/10.1016/S0065-2687(08)60052-7)
- Smith, R. B., & Kruse, C. G. (2017). Broad-spectrum mountain waves. *Journal of the Atmospheric Sciences*, 74(5), 1381–1402. <https://doi.org/10.1175/JAS-D-16-0297.1>
- Solomon, S., Rosenlof, K. H., Portmann, R. W., Daniel, J. S., Davis, S. M., Sanford, T. J., & Plattner, G.-K. (2010). Contributions of stratospheric water vapor to decadal changes in the rate of global warming. *Science*, 327(5970), 1219–1223. <https://doi.org/10.1126/science.1182488>
- Sonntag, D. (1990). Important new values of the physical constants of vapour pressure formulations based on the ITS-90, and psychrometer formulae. *Meteorologische Zeitschrift*, 40, 340–344.
- Sprenger, M., & Wernli, H. (2015). The LAGRANTO Lagrangian analysis tool—Version 2.0. *Geoscientific Model Development*, 8(8), 2569–2586. <https://doi.org/10.5194/gmd-8-2569-2015>

- Teitelbaum, H., & Sadourny, R. (1998). The role of planetary waves in the formation of polar stratospheric clouds. *Tellus A*, 50(3), 302–312. <https://doi.org/10.1034/j.1600-0870.1998.t01-2-00004.x>
- Thölix, L., Backman, L., Kivi, R., & Karpechko, A. Y. (2016). Variability of water vapour in the Arctic stratosphere. *Atmospheric Chemistry and Physics*, 16(7), 4307–4321. <https://doi.org/10.5194/acp-16-4307-2016>
- Vömel, H., Oltmans, S. J., Hofmann, D. J., Deshler, T., & Rosen, J. M. (1995). The evolution of the dehydration in the Antarctic stratospheric vortex. *Journal of Geophysical Research*, 100(D7), 13,919–13,926. <https://doi.org/10.1029/95JD01000>
- Vömel, H., Rummukainen, M., Kivi, R., Karhu, J., Turunen, T., Kyrö, E., et al. (1997). Dehydration and sedimentation of ice particles in the Arctic stratospheric vortex. *Geophysical Research Letters*, 24(7), 795–798. <https://doi.org/10.1029/97GL00668>
- Wagner, J., Dörnbrack, A., Rapp, M., Gisinger, S., Ehard, B., Bramberger, M., et al. (2017). Observed versus simulated mountain waves over Scandinavia—Improvement of vertical winds, energy and momentum fluxes by enhanced model resolution? *Atmospheric Chemistry and Physics*, 17(6), 4031–4052. <https://doi.org/10.5194/acp-17-4031-2017>
- Wedi, N. P. (2014). Increasing horizontal resolution in numerical weather prediction and climate simulations: Illusion or panacea? *Philosophical Transactions of the Royal Society B*, 372(2018), 20,130,289–20,130,289. <https://doi.org/10.1098/rsta.2013.0289>
- Wernli, H., & Davies, H. C. (1997). A Lagrangian-based analysis of extratropical cyclones. i: The method and some applications. *Quarterly Journal of the Royal Meteorological Society*, 123(538), 467–489. <https://doi.org/10.1002/qj.49712353811>
- Žagar, N., Jelić, D., Blauw, M., & Bechtold, P. (2017). Energy spectra and inertia-gravity waves in global analyses. *Journal of the Atmospheric Sciences*, 74(8), 2447–2466. <https://doi.org/10.1175/JAS-D-16-0341.1>